IOP Publishing Journal of Physics D: Applied Physics
J. Phys. D: Appl. Phys. **54** (2021) 445301 (14pp) https://doi.org/10.1088/1361-6463/ac0de5

Critical-dimension scanning electron microscope characterization of smoothly varying wave structures with a Monte Carlo simulation

M S S Khan[1], L H Yang[1], X Deng[2,*], S F Mao[3], Y B Zou[4,*], Y G Li[5], H M Li[6] and Z J Ding[1,*]

[1] Department of Physics and Hefei National Laboratory for Physical Sciences at the Microscale, University of Science and Technology of China, Hefei, Anhui 230026, People's Republic of China
[2] Institute of Precision Optics, Department of Physics, Science and Engineering, Tongji University, Shanghai 200092, People's Republic of China
[3] Department of Engineering and Applied Physics, University of Science and Technology of China, Hefei, Anhui 230026, People's Republic of China
[4] School of Physics and Electronic Engineering, Xinjiang Normal University, Urumqi, Xinjiang 830054, People's Republic of China
[5] Key Laboratory of Materials Physics, Institute of Solid State Physics, Chinese Academy of Sciences, Hefei, Anhui 230031, People's Republic of China
[6] Super Computation Center, University of Science and Technology of China, Hefei, Anhui 230026, People's Republic of China

E-mail: 1110490dengxiao@tongji.edu.cn, zyb0617@mail.ustc.edu.cn and zjding@ustc.edu.cn

Received 23 April 2021, revised 10 June 2021
Accepted for publication 23 June 2021
Published 13 August 2021

Abstract

Scanning electron microscopy (SEM) characterization of a smoothly varying nanograting structure (a Pt-coated Cr grid on a Si substrate) with a sinusoidal waveform has been carried out by a Monte Carlo (MC) simulation technique. Previous studies with critical-dimension (CD) SEM (CD-SEM) have mostly concerned line structures with sharp edges so that there is an obvious edge bloom in the linescan profile of secondary electrons. In contrast, the present grating structures prepared by a laser-focused atomic deposition technique have a smoothly varying waveform in the cross-sectional profile, which pose greater difficulty for quantitative structural characterization by SEM. The grating structure, with a fixed pitch of $\lambda/2$ as the period of the standing-wave laser light field, where λ is the wavelength of the corresponding laser light, can be used as an ideal nanoscale metrological length tool; therefore, it is important to characterize its structural features over a large deposited area by SEM imaging for quality control, with the aim of mass reproduction. The present work extends the CD characterization of MC simulation methods to more complex structures. Taking into account different experimental factors, i.e. primary electron beam parameters, geometrical parameters and material properties, the unknown geometrical parameters (i.e. base height, peak height, linewidth shrinkage and peak tilt angle) of the grating lines have been successfully extracted from the experimental linescan profiles of SEM images.

* Authors to whom any correspondence should be addressed.

Keywords: linescan, nano characterization, CD-SEM, Monte Carlo simulation, atom lithography

(Some figures may appear in colour only in the online journal)

1. Introduction

Metrology of nanoscale devices is vital for the future development of semiconductor manufacturing, new technologies and many fundamental research fields [1]. It is hoped that grating structures fabricated by an atomic lithography technique will make an ideal nanoscale metrological tool. With this technique, laser light is used as a lens to form a standing wave to focus a collimated neutral atomic beam with nanometer-scale resolution during the deposition of atoms onto a substrate [2, 3]. When passing through the array of atomic lenses, the atoms experience forces due to the tuning of the laser light near an atomic transition. The nanoscale parallel grating line structures produced by this nanofabrication technology can have an exact periodicity of half of the laser wavelength over a large (millimeter-sized) area. The nanogratings have been made of various elements, including Na [2], Cr [3–5], Yb [6], Fe [7], Al [8], Cs [9] and Ba [10]; hence, different pitches correspond to the respective wavelengths of the lasers. The most important advantage of nanostructures obtained by atomic lithography is that the pitch is very accurate and can be traced to the transition energy level of the atom and length standard, with a theoretical dimensional error caused by the uncertainty of laser frequency of <0.01 nm for a Cr nanograting. Furthermore, a maximum peak-to-valley height of over 100 nm for Cr nanogratings has been now experimentally achieved [11, 12]. Such characteristics make these nanogratings ideal for fabrication of standard nanometer length scalers, for example as a template for mass reproduction of lateral pitch standards.

However, characterization of the structural features of gratings over a large deposited area is quite tricky using conventional microscopic tools such as atomic force microscopy (AFM) and transmission electron microscopy (TEM). These are suitable for observing small areas, and the method of sample preparation for TEM is destructive. On the other hand, scanning electron microscopy (SEM) can provide observations of structural morphology over a large area of the specimen with large magnification and without a particular sample preparation procedure. Nevertheless, quantitative characterization of the structure, particularly the critical dimension (CD), by SEM is still a challenge because of the characteristic wave-type morphology of the grating line structure. Under the action of a laser dipole force, evaporated atoms will converge to the nodes or antinodes of the standing wave, depending on whether the frequency of the standing wave is higher or lower than that of the transition energy level of the atom, so that the deposited grating structures show cross-sectional profiles with a wave-type form, as observed by AFM [4–7]. This smoothly varying nanograting waveform affects the sharp contrast of the SEM image and increases the difficulty of CD characterization compared with the established method [13] for trapezoidal line structures with sharp edges in semiconductor devices. In this work, we propose the CD parameters for such a wave-type nanograting and their characterization with a Monte Carlo (MC) technique.

CD characterization on the line structures with a SEM (CD-SEM) has been comprehensively carried out, mainly for trapezoidal-like cross sections [14–25]. With the help of MC modelling, not only the linewidth but also the 3D morphological shape of the structure can be derived [26–38]. Then, the model-based library (MBL) algorithm [28, 34, 37, 39–42] can be extended to 3D metrology of the CD by including many more geometrical structure parameters, such as top CD, bottom CD, height and sidewall angles. It has been experimentally verified that this characterization method is effective even down to patterned lines with a size of 10 nm [37]. Therefore, the MBL method developed with the MC technique is also expected to be a powerful tool for the present purpose of characterizing a smoothly varying line structure. The morphological contrast in a SEM image is produced by the angular dependence of secondary electron signal emission on the angle of incidence and particularly by the edge effect [43]. Unlike the case of a trapezoidal shape, where the edge effect provides the dominant contrast, for a smooth wave-type shape the contrast is mostly due to the slope of the local surface. Image simulation can be performed by a MC tracing of electron transport and secondary electron cascade processes [44–47]. For this not only is the fundamental physical modelling of elementary electron–solid interaction required [48–51] but also suitable structure surface modelling to accommodate the need for contrast simulation.

2. Methods

2.1. Experimental

In the present study, the Cr nanograting sample was prepared by depositing Cr atoms onto a Si substrate with a laser of $\lambda = 425.6$ nm, corresponding to the $^7S_3 \rightarrow {}^7P_4^0$ transition of Cr atoms. Then for SEM observation the Cr nanograting was covered by a thin Pt film of thickness 10 nm. The pitch of this grating was $\lambda/2 = 212.8$ nm. The deposited grating area was $\sim 0.2 \times 0.5$ mm on a substrate of 3×5 mm. Figure 1(a) shows an optical microscope image of the whole nanograting sample, where A, B, C and D indicate the selected regions for our CD characterization by SEM. Each scanned region is separated vertically by 50 μm except for regions C and D. Figure 1(b) shows an enlarged image of the sample area. The

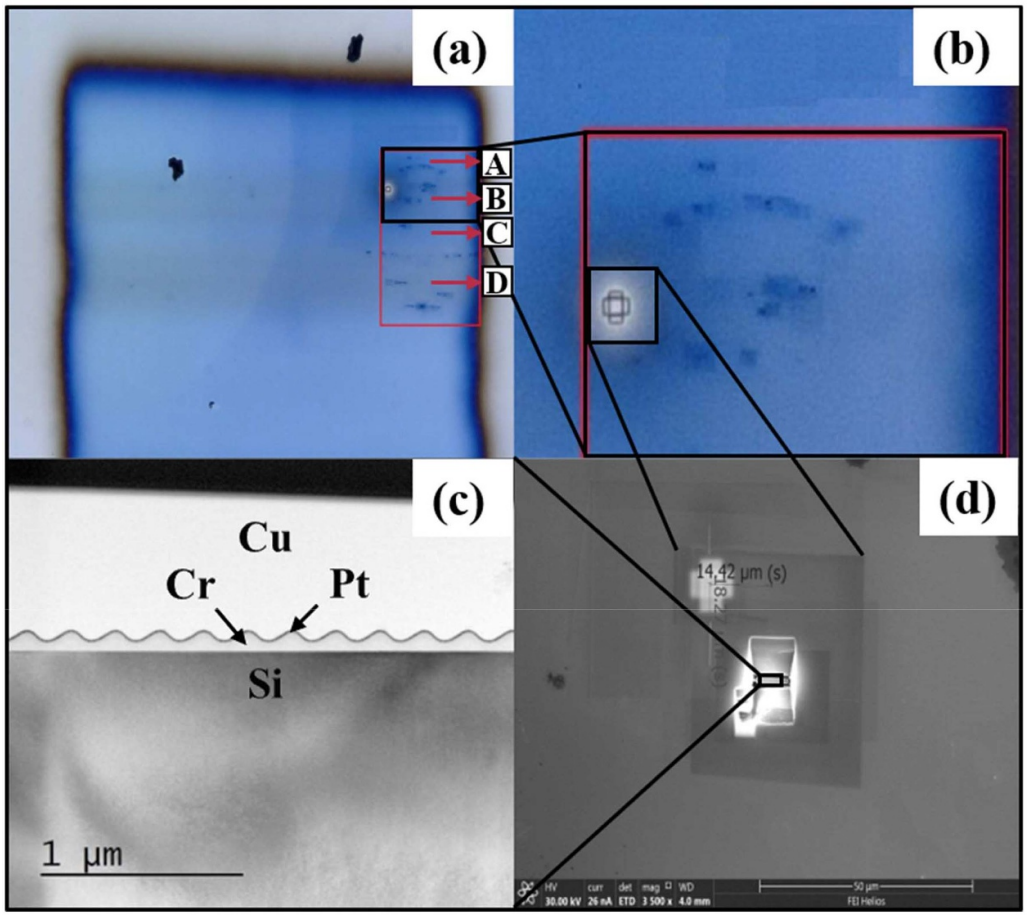

Figure 1. (a) Optical microscope image of the whole sample. A, B, C and D represent the regions of the scanned image area, where the dark smudges are due to carbon contamination by repeated electron beam scanning under the same experimental conditions as in figure 2. (b) An enlarged image of the area in (a). (c) TEM image of the cross-sectional nanograting line shape. (d) SEM image of the area for cutting a TEM sample by the etching process.

optical microscope image in figure 1(d) indicates the TEM sample area where the TEM sample is made by an etching process. Figure 1(c) is a TEM image displaying a cross-sectional view of the wave-type form for the nanograting structure. To protect the grating sample for the TEM observation, the nanograting was further covered by an additional thick Cu film.

Figures 2(a)–(d) show several selected SEM images for the most distinct contrast variations from the scanning regions A, B, C and D, and their corresponding averaged secondary electron linescan profiles. Due to the smoothly varying structure the image contrast also changes gradually; the contrast looks like a wave in figure 2(a) but has rather sharp left edges in figure 2(c). This illustrates that the structural characteristics vary with position and can be quite different over distant locations of the whole deposited nanograting sample. Such inhomogeneity cannot be easily characterized by TEM/AFM imaging. If one observes this more precisely, it can be seen that the structure even varies line by line, although the pitch ($\lambda/2$) is fixed. This inhomogeneous structural characteristic represents the fact that the atom deposition rate in practice changes slightly from place to place (and possibly from time to time) when the atomic beam from the source is evaporated onto the substrate by passing through a one-dimensional standing-wave light field.

2.2. MC simulation model

MC calculation of the SEM image is based on the computer simulation of emitted secondary electron signal intensities by tracing incident electron trajectories and the generated secondary electron trajectories inside the solid target with a random sampling technique for electron scattering events, including elastic scattering and inelastic scattering. The basic physical model and simulation procedures are described elsewhere [48, 52]. However, instead of using Penn's single-pole approximation dielectric function [53] we used the full Penn algorithm [51] to calculate electron inelastic mean free paths. A ray-tracing technique was used to calculate the electron step length [54].

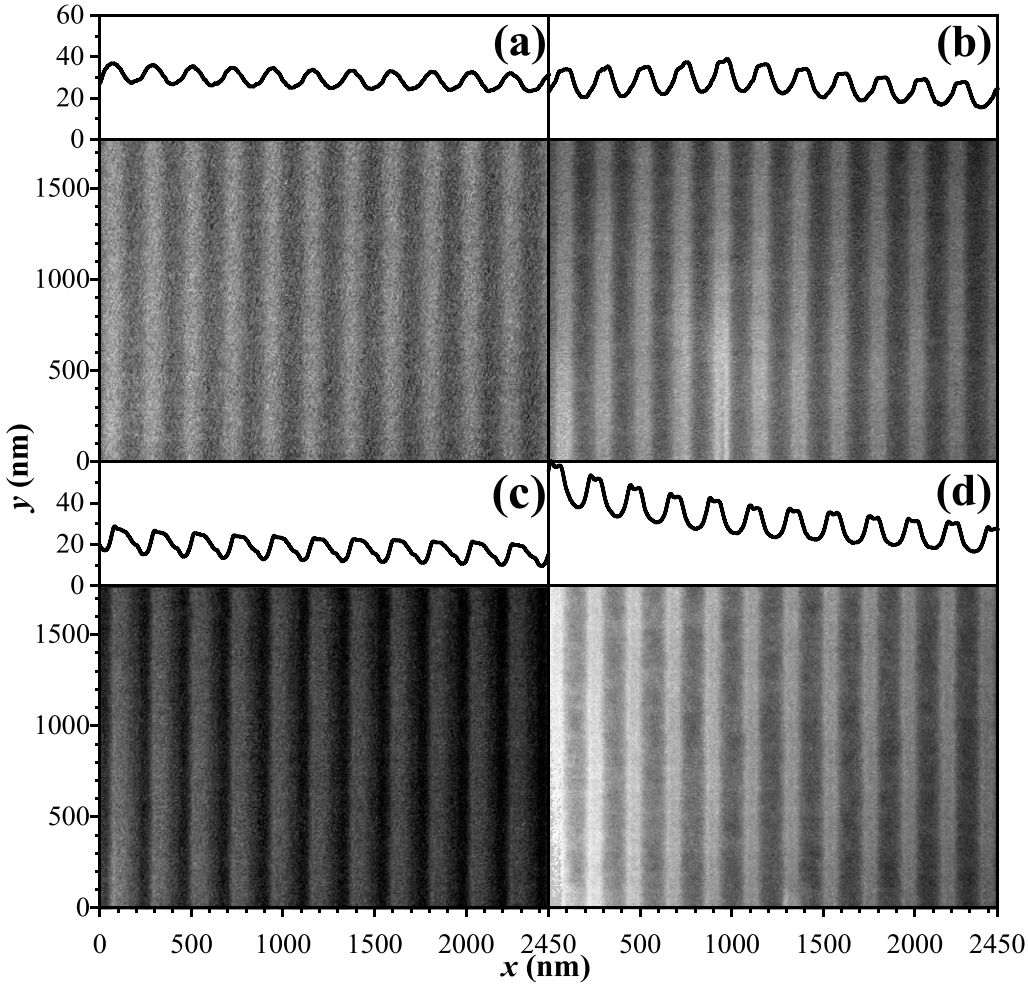

Figure 2. Experimental SEM secondary electron images (lower panels) and their corresponding averaged linescan profiles along the vertical direction of the image (upper panels) for the different scanning regions: (a) region A, (b) region B, (c) region C, (d) region D.

2.2.1. Electron elastic scattering. To deal with the electron elastic scattering, Mott's cross section [55] with the Thomas–Fermi–Dirac atomic potential was used:

$$\frac{\mathrm{d}\sigma_e}{\mathrm{d}\Omega} = |f(\theta)|^2 + |g(\theta)|^2. \tag{1}$$

Here $f(\theta)$ and $g(\theta)$ represent the scattering amplitudes; they can be obtained with a partial wave expansion method [56] as

$$f(\theta) = \frac{1}{2ik}\sum_{l=0}^{\infty}\left\{(\ell+1)\left(e^{2i\delta_\ell^+}-1\right)+\ell\left(e^{2i\delta_\ell^-}-1\right)\right\} \times P_\ell(\cos\theta), \tag{2}$$

$$g(\theta) = \frac{1}{2ik}\sum_{\ell=1}^{\infty}\left\{-e^{2i\delta_\ell^+}+e^{2i\delta_\ell^-}\right\}P_\ell^1(\cos\theta), \tag{3}$$

where δ_l^+ and δ_l^- are spin up and spin down phase shifts of the ℓth partial wave, respectively, $P_\ell(\cos\theta)$ and $P_\ell^1(\cos\theta)$ are the Legendre and first-order associated Legendre functions, respectively.

2.2.2. Electron inelastic scattering. An electron moving inside a sample interacts with other charged particles in the sample through Coulomb interaction. Excitation of the core–shell and valence electrons results in a change in the kinetic energy of a moving electron. The excitation of electrons includes a single particle mode or a collective mode.

In a dielectric function approach to electron inelastic scattering, the differential cross section calculated according to Penn's algorithm [53] is quite useful because of its broad applicability for various materials. Furthermore, using experimental optical constants, the calculation is much more accurate for realistic materials. The double differential scattering cross section is expressed in terms of the energy loss function, $\mathrm{Im}\{-1/\varepsilon(q,\omega)\}$, as

$$\frac{\mathrm{d}^2\lambda_{\mathrm{in}}^{-1}}{\mathrm{d}(\hbar\omega)\mathrm{d}q} = \frac{1}{\pi a_0 E}\mathrm{Im}\left\{\frac{-1}{\varepsilon(q,\omega)}\right\}\frac{1}{q}, \tag{4}$$

where a_0 is the Bohr radius, $\hbar\omega$ is energy loss, $\hbar q$ is the momentum transfer, E is the kinetic energy of the moving electron, $\varepsilon(q,\omega)$ is a dielectric function of the solid and $\lambda_{\mathrm{in}}^{-1}$ is the electron inelastic mean free path. We have used the full Penn

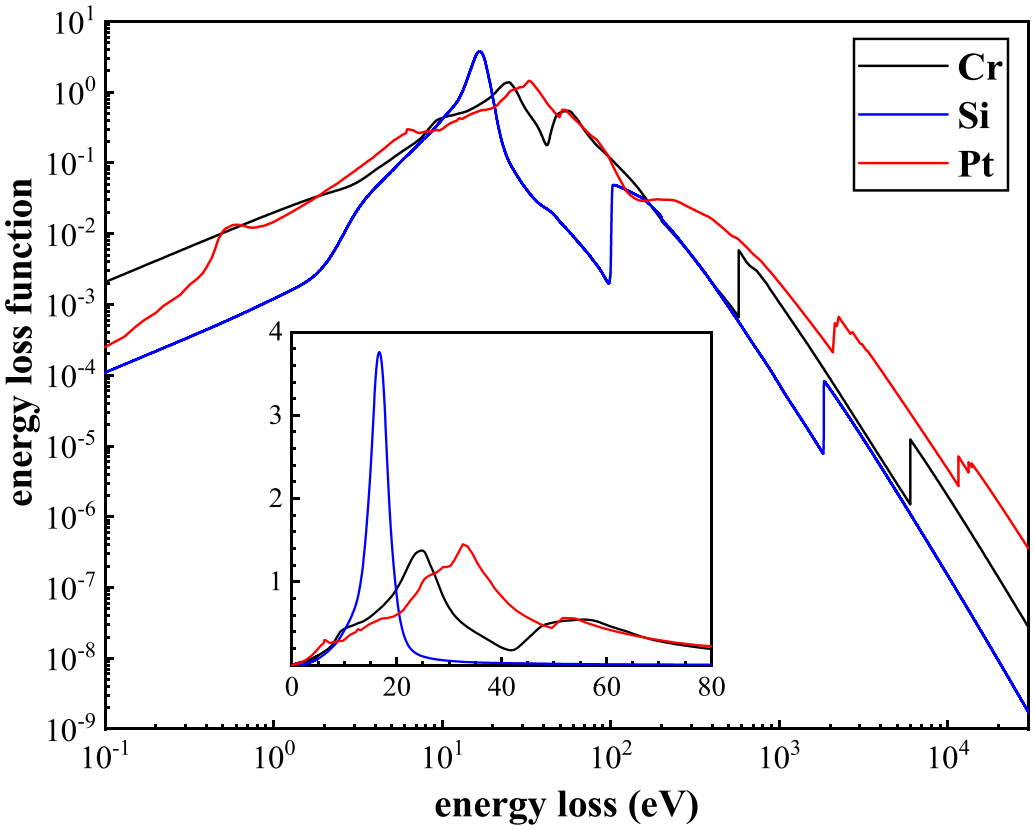

Figure 3. Optical energy loss functions, $\mathrm{Im}\{-1/\varepsilon(\omega)\}$, of Cr, Si and Pt used in the simulations.

algorithm [51] instead of the conventional single-pole approximation to calculate the energy loss function. The energy loss function is expanded as

$$\mathrm{Im}\left\{\frac{-1}{\varepsilon(q,\omega)}\right\} = \int_0^\infty g(\omega_p)\,\mathrm{Im}\left\{\frac{-1}{\varepsilon_L(q,\omega;\omega_p)}\right\} d\omega_p, \quad (5)$$

where $g(\omega_p)$ is the expansion coefficient, which is obtained from the optical energy loss function as $g(\omega) = (2/\pi\omega)\,\mathrm{Im}\{-1/\varepsilon(\omega)\}$. $\varepsilon_L(q,\omega;\omega_p)$ is Lindhard dielectric function of free electron gas having plasmon energy $\hbar\omega_p$. Since $\varepsilon(\omega)$ is related to the optical constants, which have been experimentally measured over a wide photon energy range and for a variety of materials, the differential cross section can be conveniently calculated, and its integration leads to the energy loss distribution and angular distribution for MC simulation. In this work, the optical constants of Cr and Si are extracted from the results of reflection electron energy loss spectroscopy [57, 58] in the energy loss range of 0–200 eV and determined from the atomic scattering factor [59] in the range of $\hbar\omega > 200$ eV. The optical constants of Pt are taken from Palik [60] in the range of 0.1–82.66 eV and determined from the atomic scattering factor [59] in the range of $\hbar\omega > 95$ eV. Figure 3 shows the optical energy loss functions, $\mathrm{Im}\{-1/\varepsilon(\omega)\}$, of the three materials used in the present simulations.

2.3. Geometric model

As an essential input for a SEM image simulation, a geometrical model of the specimen is specified by the shape of its boundaries and properties of the materials contained inside because the secondary electron yield relies on the specimen [61]. Various methods of structural modelling, such as constructive solid geometry [62, 63], finite element triangular mesh (FETM) [36, 54, 64], height maps [37] and tetrahedral mesh [65], have been employed. Here we employ the FETM method to construct a smooth structural surface for the input to our CTMC-3DSEM simulation of complex 3D sample geometries [66]. To minimize the computation time, which increases with the number of triangles in the mesh, we have adopted the optimization technique of space subdivision [67]. This optimization technique will accelerate our calculation. We have employed Gmsh [68], freely available meshing software, for the construction of a 3D closed mesh.

To create the numerical coordinates for meshing the wave-type form of the model structure, we employed the modified sinusoidal function

$$\begin{cases} x(t) = t + h\sin^2(\omega t/2)\tan\theta + s\sin\omega t; \\ z(t) = h\sin^2(\omega t/2) + b, \end{cases} \quad (6)$$

where $\omega = 4\pi/\lambda$ and t is a variable to generate coordinates. h is the peak height (peak-to-valley height), b is the base height (valley-to-substrate height), $2s$ is the linewidth

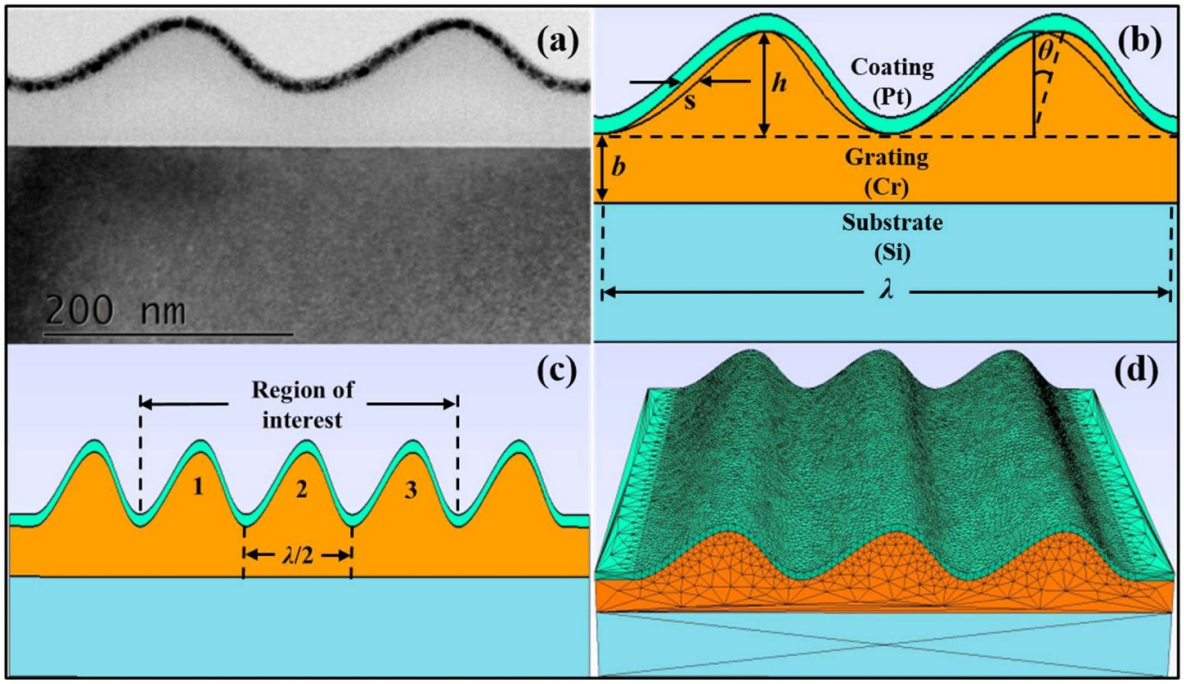

Figure 4. (a) Enlarged TEM image of the cross-sectional grating shape showing the wave type morphology of the deposited Cr film. (b) Schematic diagram of the geometric model, where $\lambda/2$ is the period of the wave structure, h is peak height, b is the base height, $2s$ is the linewidth shrinkage and θ is the tilt angle of a wave peak. The structural model includes four layers: Si (substrate), Cr (grating), Pt (coating) and vacuum. (c) Schematic diagram of the five-line sample structure considered for the MC simulation. (d) The 3D mesh continuation of the geometric model having dimensions of 1175 nm $\times$ 1175 nm and $\sim$(4–5) $\times$ 10^5 triangles.

shrinkage (the length narrowed or squeezed from the middle of ideal sinusoidal waveform) and θ is the tilt angle of the wave peak. The main structural parameter, i.e. the linewidth w or CD estimated by the full width at half maximum (FWHM), can be obtained as $w = \lambda/4 - 2s$. Other important CD parameters are h and θ.

Figure 4 shows line structure modelling. Figure 4(b) schematically illustrates the model, which follows the line shape as displayed in the experimental TEM image in figure 4(a). Three layers of different elements (Pt, Cr and Si) in addition to a vacuum are considered so that in the simulation code several different interfaces need to be taken into account in tracing the electron trajectories. Figure 4(c) shows a cross-sectional view of the modelled 3D structure, which has five wave peaks in total; we have scanned the three middle wave peaks to take into account the effect of the neighbouring structure. Hence, the overall dimension of structure in the xy-plane is 1175 nm $\times$ 1175 nm in the simulation of the SEM linescan profile. After creating these surfaces, we applied adaptive-mesh 2D triangular meshes to these surfaces, as shown in figure 4(d), and the total number of triangles in the 3D triangular mesh of the line structure is $\sim$(4–5) $\times$ 10^5.

3. Results and discussion

Figure 5 demonstrates the simulated electron trajectories, including incident electrons and their generated cascade electrons near the surface. The primary beam of 4 keV and 10 keV incident energies is either incident on the side slope or at the valley of the wave structure in the illustration. One can observe that at 10 keV (figures 5(b) and (d)) incident electrons can penetrate much deeper inside the structure, and backscattered electrons (black arrows) can be emitted from the wider nearby region about the incident position so that the secondary electrons are produced more widely in the lateral direction, representing the stronger neighbouring effect; in comparison, at 4 keV (figures 5(a) and (c)) secondary signals (red arrows) are more local to the incident position and the neighbouring effect is comparatively smaller. When the primary beam is incident at the peak side of the wave structure (figures 5(a) and (b)) more secondary electrons are emitted from the side slope, while in the case of a beam incident at the valley position (figures 5(c) and (d)) secondary electron emission is depressed due to absorption by the curvature of the structure near the valley.

In the spirit of the MBL, we then performed a series of MC simulations of linescan profiles for many combinations of parameter set values. In each calculation the linescan profile consisted of 168 scanning pixels for a three-line structure; we traced 1 $\times$ 10^5 incident electron trajectories and several dozen secondary electron trajectories for each pixel. The five-line structure in figure 4(c) is considered because some emitted backscattered electrons and high-energy secondary electrons may further hit the nearby structure and produce more low-energy secondary electrons. The secondary electron emission

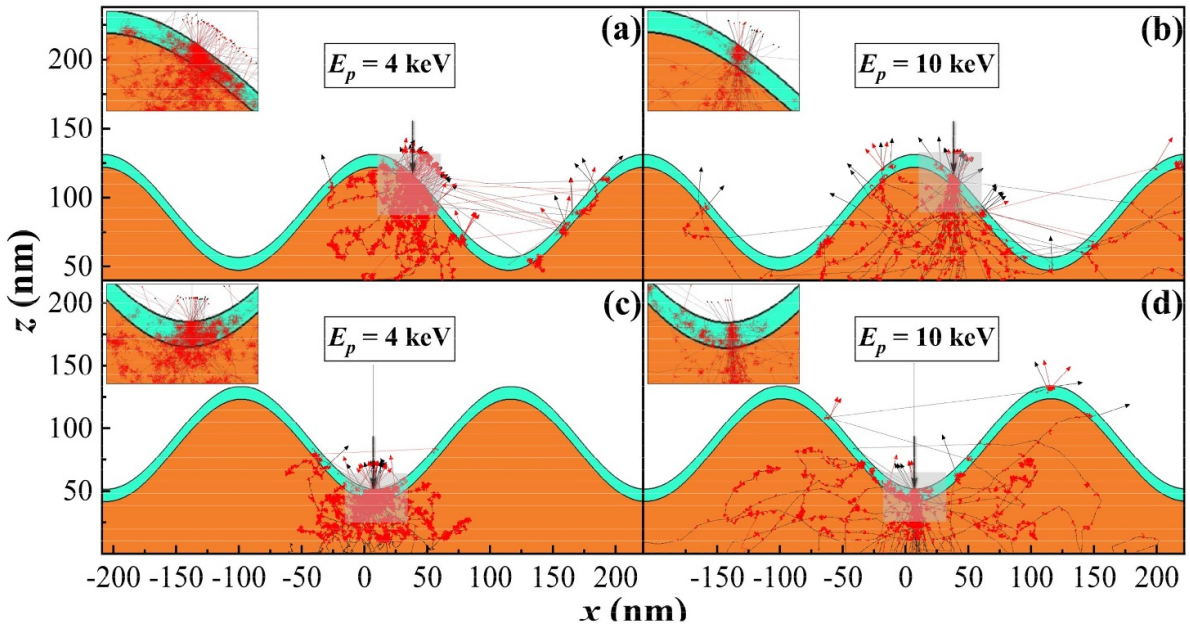

Figure 5. Scattering trajectories of 50 primary electrons (black) and their corresponding cascade secondary electrons (red) at the midpoint of the side slope of wave structure for beam energies of (a) 4 keV and (b) 10 keV, and at the valley point for beam energies of (c) 4 keV (d) 10 keV. The thick black arrows indicate the incident electron beam, and the zoomed images show the generated and emitted secondary electron trajectories in the rectangular region near the impact points. Other parameters, i.e. peak height $h = 132$ nm, base height $b = 41.5$ nm, peak tilt angle $\theta = 0^\circ$, linewidth shrinkage $2s = 0$, incident angle $\beta = 0^\circ$ and beam size (FWHM) $= 0$ nm, are kept constant.

yield is counted as the intensity of the linescan profile. Figure 6 shows a comparison between the experimental and final simulated linescan profiles at a primary beam energy of 10 keV for scanning positions at four different regions, A, B, C and D, of the sample in figure 1(a). By least-squares fitting of the linescan profiles between the experimental and simulated ones corresponding to the different parameter set values considered, we obtained the best-fit structural parameters for the selected wave-type Cr grating lines in the SEM image of figure 2. The line structure parameters are described in the right panel of figure 6 for each wave peak. By carefully observing the linescan profiles of the experimental 2D SEM images, we found that the pitch value, 215.7 nm, is indeed exactly fixed for consecutive waves. However, the pitch value measured directly with a conventional SEM scale does not agree with the value of $\lambda/2 = 212.8$ nm. This simply represents the fact that the SEM scale has a relative error of 1.36% compared with the Cr grating pitch, which has a metrological traceability to the light wavelength standard. Calibration of the length quantities, i.e. *h, b, s* (and hence, *w*), measured from the SEM image can then be done with a scaling factor of 0.98656. We have noted that the quantitative values of the line structure parameters *h, b, s* (and hence, *w*) and θ vary from region to region, and even from line to line.

The typical inhomogeneity of the sample structure can be clearly seen from the selected linescan profiles in figure 2. For example, figure 2(c) shows asymmetric lines, figure 2(b) shows a change of line structure along the vertical direction for a single line and figure 2(d) shows strong brightness reducing from left side to the right side. The corresponding change in structural parameters can be derived from the image simulation. Figure 6 treats only a particular example of three lines. In figure 6(a), there is only a minor tilt for the left peak, linewidth $w \approx 181$ nm and height $h \approx 60$ nm. In figure 6(b), the peak is slightly tilted to the right, and the base height is increased from left to right, $w \approx 189$ nm and $h \approx 92$ nm for the right peak. In figure 6(c), the peak is strongly tilted to the left by $\sim 8^\circ$, $w \approx 193$ nm and $h \approx 95$ nm for the left peak. In figure 6(d), the peak is somewhat tilted to the left by $\sim 3^\circ$ while the base height and peak height are both reduced from left to right, $w \approx 185$ nm and $h \approx 90$ nm for the left peak. However, the structural modelling shown in the right panels of figure 6 demonstrates much less obvious changes in the structure compared with the changes in the intensity profiles of secondary emission shown in the left panel. This is due to the inverse cosine law $1/\cos^n\alpha$ of the angular dependence of secondary electron emission, where α is the angle between the incident electron direction and local surface normal and n varies from 1.3 for light elements to 0.8 for heavy elements. This angular dependence will enhance the effect of local surface tilt to present a morphological contrast. Therefore, the larger slope of the peak side surface, which is estimated from the aspect ratio h/w, in figures 6(c) and (d), as compared with figure 6(a), leads to the two humps in the linescan profiles in figures 6(c) and (d). The humps in the linescan profiles in figure 6 are quite similar to those that appear at the sharp edges for a trapezoidal line structure, but now the concerned structure has a smooth surface curvature instead of sharp edges. The phenomena look similar, but their causes are somewhat different. At a certain aspect ratio, the two side humps merge to one single peak

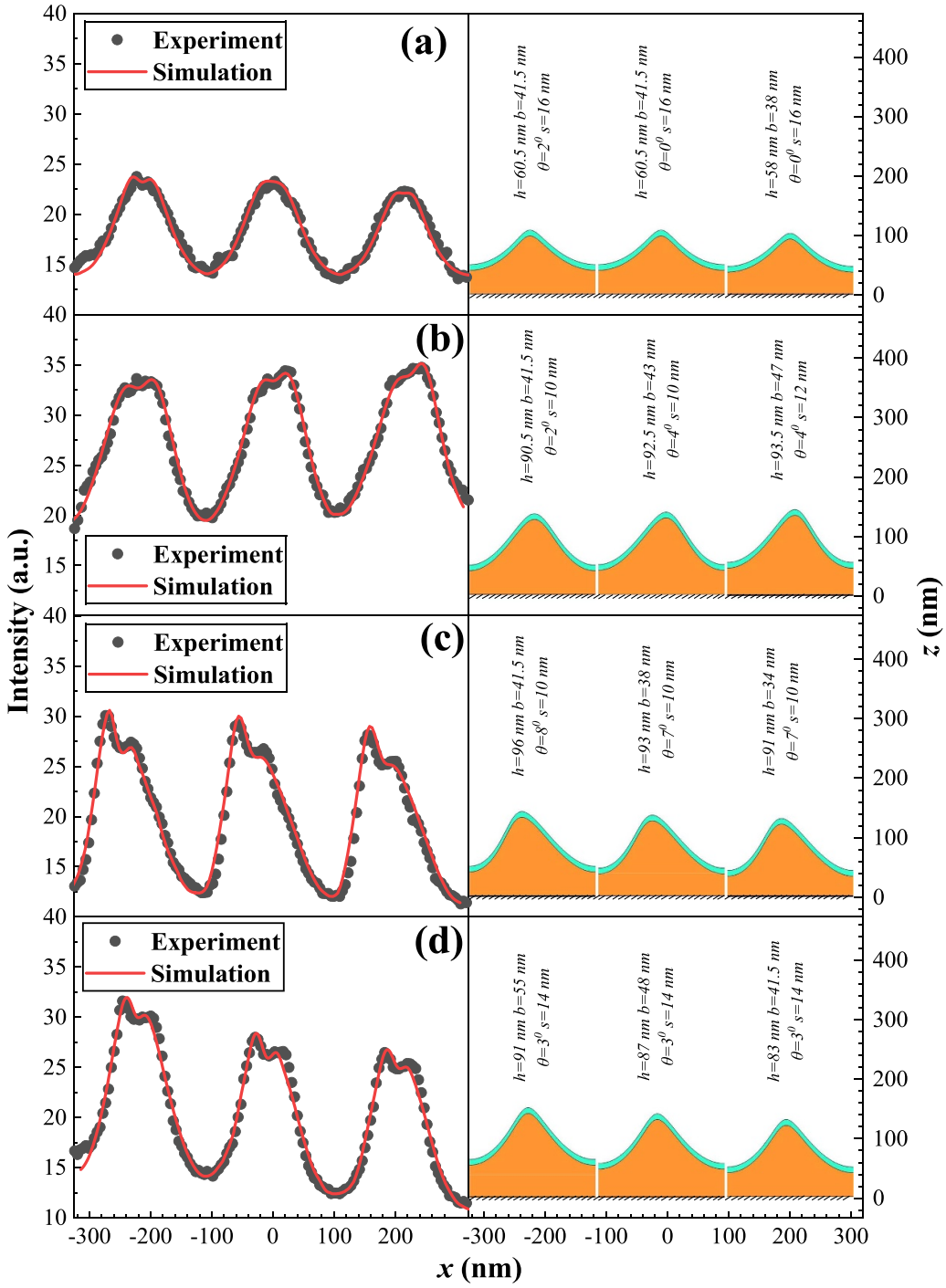

Figure 6. Left panels: comparison between the simulated and experimental linescan profiles for the scanning positions (a) region A, (b) region B, (c) region C and (d) region D. Right panels: the corresponding structural models for the simulation. All the lengths were measured directly with the SEM scale, and the true values should be scaled with a factor of 0.98656.

entirely at the centre of the peak [69]. Therefore, what we have observed is the side effect, for which the emission has the maximum intensity around the middle of the side slope of the wave peak, contrary to the edge effect in the case of a trapezoidal line shape. When the wave peak is tilted towards one side, then the hump at this side in the peak of linescan profile is higher than that at the other side. However, it should be noted that the effect of surface carbon contamination, as can be seen from figure 1(b), has not been included in the present study. Because n is quite different for C and Pt, the carbon contamination will enhance the side effect in the linescan profile; then, the structural inhomogeneity would be reduced after taking into account the contamination.

Due to the limitations of sample preparation, one can observe only a few line structures by TEM. In contrast, SEM can provide structural information in a relatively wide field.

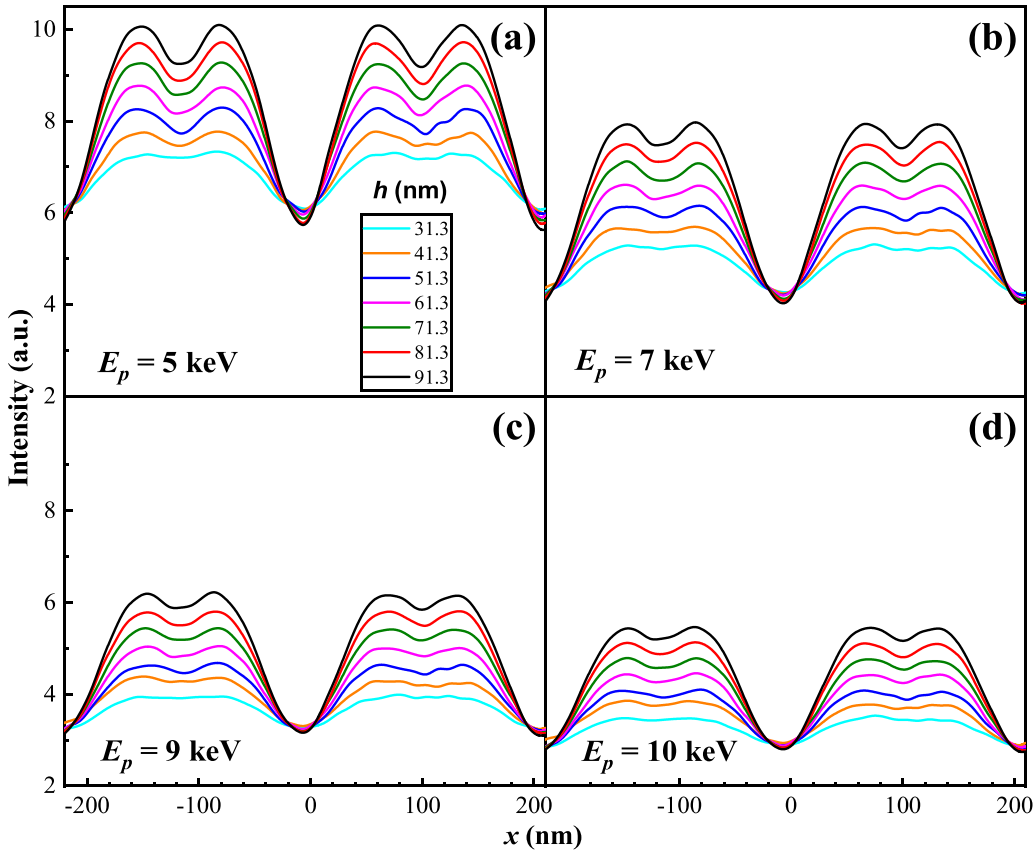

Figure 7. Simulated dependences of linescan profiles on the peak height h for the selected beam energy E_p: (a) 5 keV, (b) 7 keV, (c) 9 keV, (d) 10 keV. Other parameters, i.e. base height $b = 41.5$ nm, peak tilt angle $\theta = 0°$, linewidth shrinkage $2s = 0$, incident angle $\beta = 0°$ and beam size (FWHM) = 1 nm, are kept constant.

The structural information is contained in the image contrast or the linescan profile of a secondary electron SEM image. Using a geometrical model in our up-to-date MC simulation, we are able to predict the effect of the experimental parameters, including the beam and geometrical parameters.

Figure 7 shows the effect of peak height h on the simulated linescan profiles for several selected beam energies with all other geometrical and beam parameters being kept constant. One can observe that the profile shape, as well as linescan intensity, depends on the peak height of the wave structure, particularly at lower beam energies. The two humps in the case of a large peak height, where the maxima appear around the middle of the side slope of the wave structure, represent a prominent side effect instead of the edge effect of a trapezoidal structure. This can be explained by the inverse cosine law, $1/\cos^n\alpha$, of the angular dependence of secondary electron emission on the local angle of incidence [43], where α is the angle between the incident electron direction and local surface normal and n is a material-dependent constant. For a plane surface, α equals the incident angle β; however, it varies with the local surface curvature for the present wave structure. Near the peak top and valley bottom regions, the local incident angle is small, while it is largest at the middle of the slope. By decreasing the peak height, the side slope and the maximum local incident angle reduce; this results in smaller SE emission intensity. Furthermore, although a significant number of primary electrons can penetrate from the structure to the substrate, almost all the secondary electrons are emitted from the top surface region around 1 nm [47]. Therefore, the substrate plays only a minor role in the emission intensity.

Similarly, figure 8 shows the simulated linescan profiles for several selected peak tilt angles θ with all other geometrical and beam parameters being kept constant. The wave peak is tilted clockwise by several degrees and the waveform is thus asymmetric. One can see that the right side peak is higher than the left side peak, and this variation tendency increases with θ. The change in the linescan profiles can be understood from the angular dependence of secondary electron emission on the local incident angle: the slope of the right side is larger than the left side.

To observe the effect of the incident angle β on the linescan profile, figure 9 shows the simulated linescan profiles for several selected incident angles β in an anticlockwise direction while keeping all other geometrical and beam parameters constant. By comparing figure 9 with figure 8, one can see that the effect of the incident angle is almost the same as that of the peak tilt angle. Figure 10 shows a further detailed comparison. A difference between the incident angle and peak tilt angle appears for large angles greater than 5°. At 10°, not only the intensity but also the peak position differs.

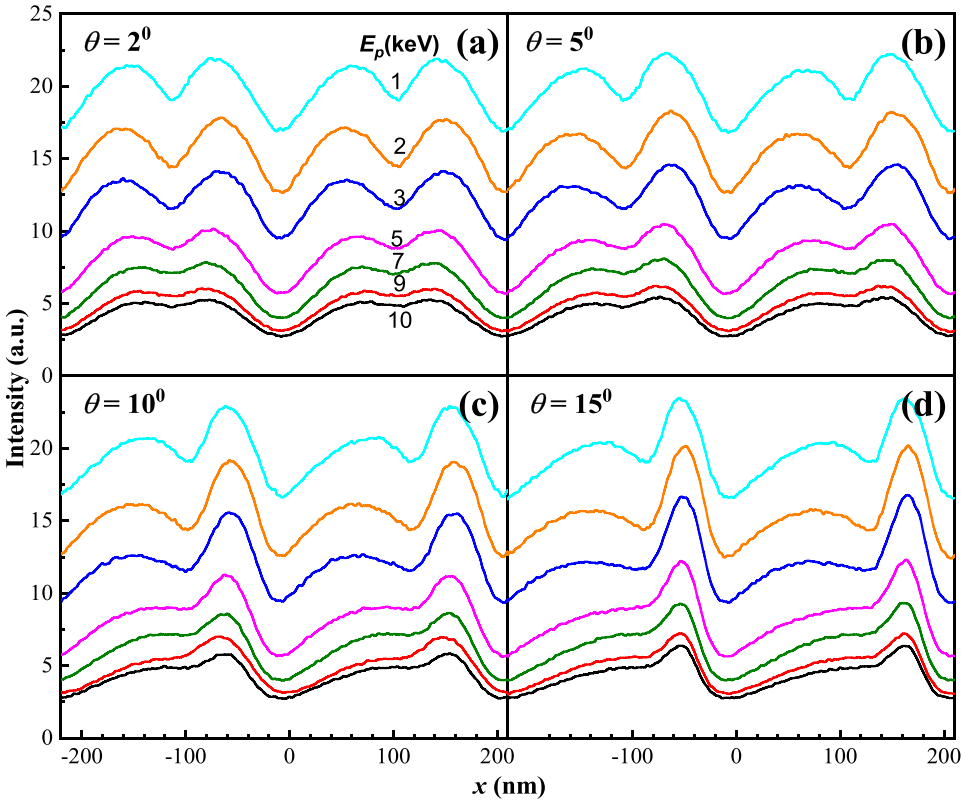

Figure 8. Simulated dependences of linescan profiles on the beam energy E_p for the selected peak tilt θ in a clockwise direction: (a) 2°, (b) 5°, (c) 10°, (d) 15°. Other parameters, i.e. peak height $h = 81.3$ nm, base height $b = 41.5$ nm, incident angle $\beta = 0°$, linewidth shrinkage $2s = 0$, incident angle $\beta = 0°$ and beam size (FWHM) = 1 nm, are kept constant.

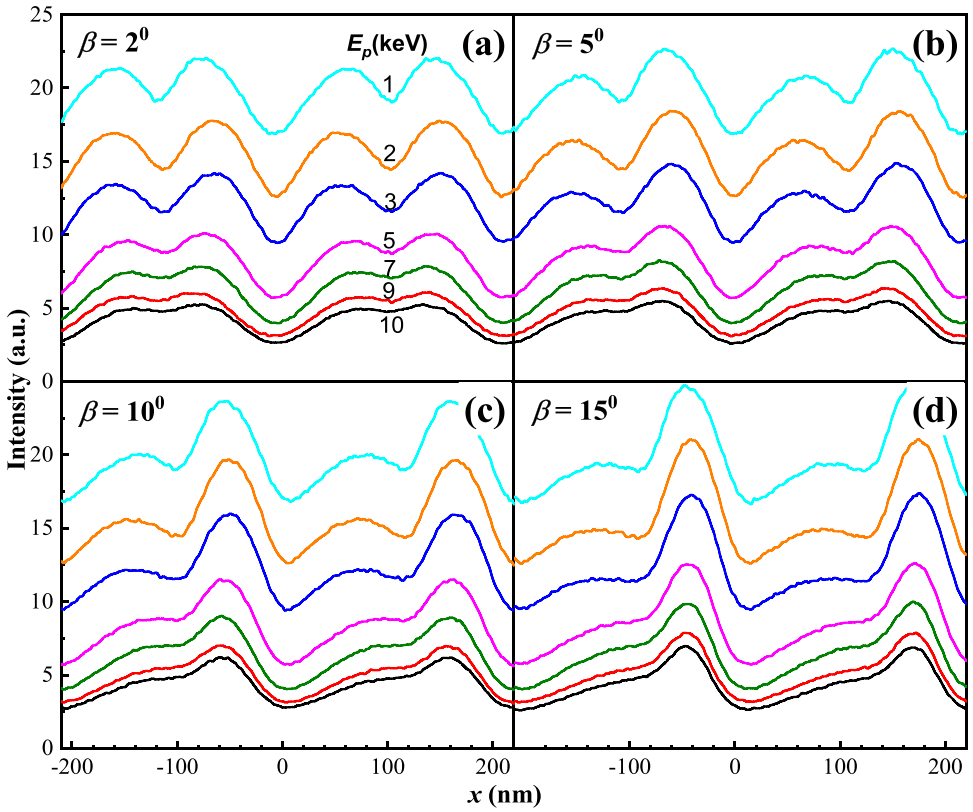

Figure 9. Simulated dependences of linescan profiles on the beam energy E_p for the selected incident beam β: (a) 2°, (b) 5°, (c) 10°, (d) 15°. Other parameters, i.e. peak height $h = 81.3$ nm, base height $b = 41.5$ nm, peak tile angle $\theta = 0°$, linewidth shrinkage $2s = 0$ and beam size (FWHM) = 1 nm, are kept constant.

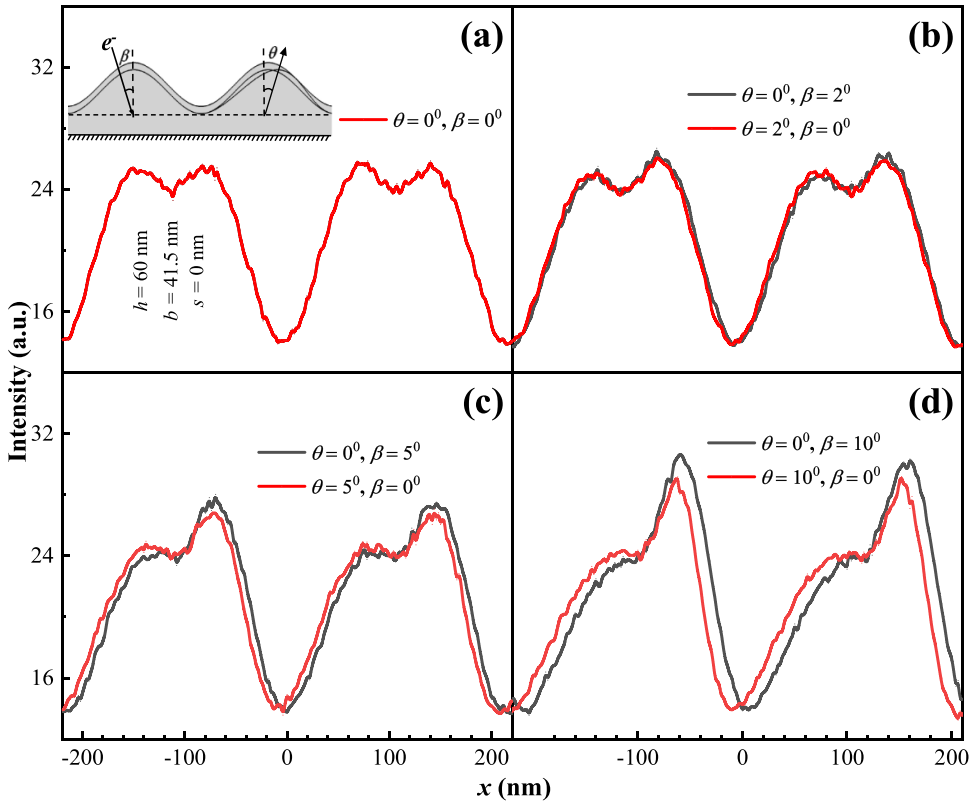

Figure 10. Comparison of the simulated linescan profiles for different peak tilt angle θ (clockwise) and incident angle β (anticlockwise): (a) $\theta = 0^\circ$ and $\beta = 0^\circ$; (b) $\theta = 0^\circ$ and $\beta = 2^\circ$, $\theta = 2^\circ$ and $\beta = 0^\circ$; (c) $\theta = 0^\circ$ and $\beta = 5^\circ$, $\theta = 5^\circ$ and $\beta = 0^\circ$; (d) $\theta = 0^\circ$ and $\beta = 10^\circ$, $\theta = 10^\circ$ and $\beta = 0^\circ$. Other parameters, i.e. peak height $h = 60$ nm, base height $b = 41.5$ nm, linewidth shrinkage $2s = 0$, beam energy $E_p = 10$ keV and beam size (FWHM) $= 1$ nm, are kept constant.

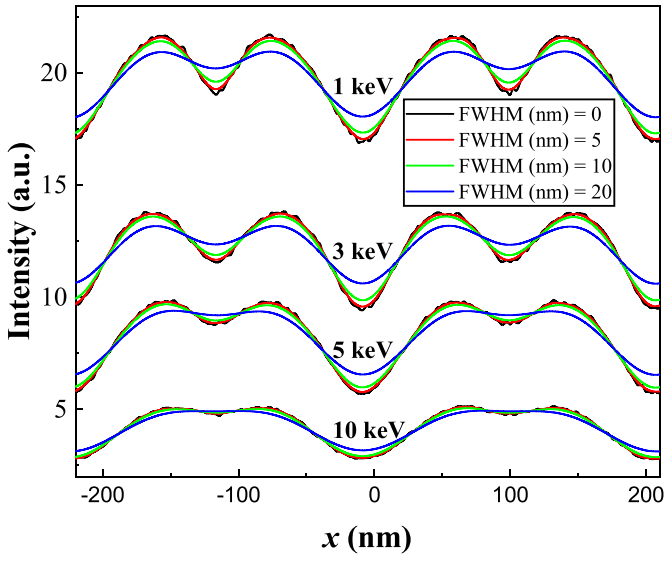

Figure 11. Simulated dependences of linescan profiles on the beam size (FWHM) for selected beam energies of 1, 3, 5 and 10 keV. Other parameters, i.e. peak height $h = 132$ nm, base height $b = 41.5$ nm, peak tilt angle $\theta = 0^\circ$, linewidth shrinkage $2s = 0$ and incident angle $\beta = 0^\circ$, are kept constant.

The beam parameters are important factors in the measurement of CD-SEM images. Beam energy, probe size and shape, incident angle and so forth can affect the signal intensity and CD-SEM contrast in different ways. In CD-SEM, the lateral resolution is also governed by the probe size [70, 71]. To illustrate the influence of beam width on CDs in detail, the line scans of the wave structure at different beam energies and probe sizes are shown in figure 11. The electron probe is modelled by the Gaussian profile which is characterized by the FWHM. One can observe that the contrast in the linescan decreases with increase in the beam energy. However, the CDs seem to be nearly the same at different beam energies. However, one can observe that the probe size has a significant influence on the CDs. It has been pointed out that the beam shape may not be correctly described by the simple Gaussian model [72], and that the effect of incident angle is not negligible; the electron distribution far from focus is also not consistent with a Gaussian model at the impact position of electrons on the line due to the effect of aberrations of the beam shape. Therefore, a better beam shape model is required for more accurate measurement of structural parameters by CD-SEM.

4. Conclusion

In this work, we have demonstrated that the SEM image and linescan profile for a complex sample structure having a smooth varying structural surface and in the form of multilayered materials can be quantitatively characterized by an MC simulation method to gvie the 3D morphological parameters with considerable success. Due to the side effect

of secondary electron emission from the waveform structure, the linescan profile can present a peak at the position for the maximum of the slope. This side effect enables quantitative characterization of the 3D morphological parameters for the waveform structure. Other experimental factors, for example the electron beam size and shape, focusing [73] and the incident angle, that may alter the shape of the linescan profile can also be included in the simulation for improved structural characterization.

Data availability statement

The data that support the findings of this study are available upon reasonable request from the authors.

Acknowledgments

This work was supported by the National Key Research and Development Project (2019YFF0216404 and 2019YFF0216401), National Natural Science Foundation of China (Nos. 11864041, 11975018 and 11775254), National MCF Energy R&D Program (No. 2018YEF0308100), Science Challenge Project (No. TZ2018004), Youth Innovation Promotion Association CAS (outstanding member) and Chinese Education Ministry through the '111' Project 2.0 (BP0719016).

ORCID iDs

M S S Khan https://orcid.org/0000-0001-7723-2887
L H Yang https://orcid.org/0000-0002-5948-7736
S F Mao https://orcid.org/0000-0002-2370-1585
Y B Zou https://orcid.org/0000-0002-0572-1726
Y G Li https://orcid.org/0000-0003-2820-2424
Z J Ding https://orcid.org/0000-0001-5767-1145

References

[1] Vogel E 2007 Technology and metrology of new electronic materials and devices *Nat. Nanotechnol.* **2** 25
[2] Timp G, Behringer R E, Tennant D M, Cunningham J E, Prentiss M and Berggren K K 1992 Using light as a lens for submicron, neutral-atom lithography *Phys. Rev. Lett.* **69** 1636
[3] McClelland J J, Scholten R E, Palm E C and Celotta R J 1993 Laser-focused atomic deposition *Science* **262** 877
[4] McClelland J J and Celotta R J 2000 Laser-focused atomic deposition–nanofabrication via atom optics *Thin Solid Films* **367** 25
[5] Chen J, Liu J, Wang X, Zhang L, Deng X, Cheng X and Li T 2017 Optimization of nanograting pitch evaluation method based on line edge roughness analysis *Meas. Sci. Rev.* **17** 264
[6] Ohmukai R, Urabe S and Watanabe M 2003 Atom lithography with ytterbium beam *Appl. Phys.* B **77** 415
[7] Sligte T E, Smeets B, Van Der Stam K M R, Herfst R W, Van Der Straten P, Beijerinck H C W and Van Leeuwen K A H 2004 Atom lithography of Fe *Appl. Phys. Lett.* **85** 4493
[8] McGowan R W, Giltner D M and Lee S A 1995 Light force cooling, focusing, and nanometer-scale deposition of aluminum atoms *Opt. Lett.* **20** 2535
[9] Camposeo A, Cervelli F, Tantussi F, Lindholdt M, Fuso F, Allegrini M and Arimondo E 2003 Atomic nanofabrication by laser manipulation of a neutral cesium beam *Mater. Sci. Eng.* C **23** 1087
[10] Fioretti A, Camposeo A, Tantussi F, Arimondo E, Gozzini S and Gabbanini C 2005 Atomic lithography with barium atoms *Appl. Surf. Sci.* **248** 196
[11] McClelland J J, Anderson W R, Bradley C C, Walkiewicz M, Celotta R J, Jurdik E and Deslattes R D 2003 Accuracy of nanoscale pitch standards fabricated by laser-focused atomic deposition *J. Res. Natl Inst. Stand. Technol.* **108** 99
[12] Chen J, Liu J, Zhu L, Deng X, Cheng X and Li T 2018 Optimization of atom flux in atom lithography *Acta Opt. Sin.* **38** 1202001
[13] ISO 21466:2019(E) 2019 *Microbeam Analysis—Scanning Electron Microscopy—Method for Evaluating Critical Dimensions by CD-SEM* (released www.iso.org/standard/70944.html)
[14] Villarrubia J S, Vladár A E, Lowney J R, Postek M T, Allen R A, Cresswell M W and Ghoshtagore R N 2000 Linewidth measurement intercomparison on a BESOI sample *Proc. SPIE* **3998** 84
[15] Shishido C, Takagi Y, Tanaka M, Komuro O, Morokuma H and Sasada K 2002 Characterizing cross-sectional profile variations by using multiple parameters extracted from top-down SEM images *Proc. SPIE* **4689** 653
[16] Morokuma H, Miyamoto A, Tanaka M, Kazui M and Takane A 2004 New technique to reconstruct effective 3D profile from tilt images of CD-SEM *Proc. SPIE* **5375** 727
[17] Onozuka T, Ojima Y, Meessen J and Rijpers B 2006 Estimation of pattern shape based on CD-SEM image by using MPPC method *Proc. SPIE* **6152** 61521D
[18] Tanaka M, Shishido C and Kawada H 2006 Influence of electron incident angle distribution on CD-SEM linewidth measurements *Proc. SPIE* **6152** 61523Z
[19] Frase C G, Buhr E and Dirscherl K 2007 CD characterization of nanostructures in SEM metrology *Meas. Sci. Technol.* **18** 510
[20] Babin S, Bay K and Hwu J J 2010 Application of analytic scanning electron microscopy to critical dimensions metrology at nanometer scale *J. Vac. Sci. Technol.* B **28** C6H1
[21] Postek M T and Vladár A E 2011 Modeling for accurate dimensional scanning electron microscope metrology: then and now *Scanning* **33** 111
[22] Ueda K, Koshihara S, Mizuno T and Miura A 2011 The study of high-sensitivity metrology method by using CD-SEM *Proc. SPIE* **7971** 797124
[23] Häßler G W, Hüser D, Johnsen K P, Frase C G and Bosse H 2011 Current limitations of SEM and AFM metrology for the characterization of 3D nanostructures *Meas. Sci. Technol.* **22** 94003
[24] Postek M T and Vladár A E 2013 Does your SEM really tell the truth?—How would you know? Part 1 *Scanning* **35** 355
[25] Bunday B, Cepler A, Cordes A and Arceo A 2014 CD-SEM metrology for sub-10nm width features *Proc. SPIE* **9050** 90500T
[26] Davidson M P and Sullivan N 1995 Monte-Carlo simulation for CD-SEM calibration and algorithm development *Proc. SPIE* **2439** 334
[27] Davidson M P and Vladár A E 1999 Inverse scattering approach to SEM linewidth measurements *Proc. SPIE* **3677** 640

[28] Gorelikov D V, Remillard J, Sullivan N T and Davidson M 2005 Model-based CD-SEM metrology at low and ultralow landing energies: implementation,and results for advanced IC manufacturing *Surf. Interface Anal.* **37** 959

[29] Frase C G and Häßler G W 2005 Use of Monte Carlo models in the development and validation of CD operators *Surf. Interface Anal.* **37** 942

[30] Villarrubia J S, Vladár A E and Postek M T 2005 Scanning electron microscope dimensional metrology using a model-based library *Surf. Interface Anal.* **37** 951

[31] Villarrubia J S, Ritchie N W M and Lowney J R 2007 Monte Carlo modeling of secondary electron imaging in three dimensions *Proc. SPIE* **6518** 65180K

[32] Tanaka M, Shishido C, Nagatomo W and Watanabe K 2008 Application of model-based library approach to Si_3N_4 hardmask measurements *Proc. SPIE* **6922** 69222L

[33] Villarrubia J S and Ding Z J 2009 Sensitivity of SEM width measurements to model assumptions *Proc. SPIE* **7272** 72720R

[34] Frase C G, Gnieser D and Bosse H 2009 Model-based SEM for dimensional metrology tasks in semiconductor and mask industry *J. Phys. D: Appl. Phys.* **42** 183001

[35] Ciappa M, Koschik A, Dapor M and Fichtner W 2010 Modeling secondary electron images for linewidth measurement by critical dimension scanning electron microscopy *Microelectron. Reliab.* **50** 1407

[36] Li Y G, Zhang P and Ding Z J 2013 Monte Carlo simulation of CD-SEM images for linewidth and critical dimension metrology *Scanning* **35** 127

[37] Villarrubia J S, Vladár A E, Ming B, Kline R J, Sunday D F, Chawla J S and List S 2015 Scanning electron microscope measurement of width and shape of 10 nm patterned lines using a JMONSEL-modeled library *Ultramicroscopy* **154** 15

[38] Zou Y B, Khan M S S, Li H M, Li Y G, Li W, Gao S T, Liu L S and Ding Z J 2018 Use of model-based library in critical dimension measurement by CD-SEM *Measurement* **123** 150

[39] Shishido C, Tanaka M and Osaki M 2010 CD bias reduction in CD-SEM of very small line patterns: sidewall shape measurement using model-based library matching method *Proc. SPIE* **7638** 76383I

[40] Yasui N, Isawa M, Ishimoto T, Sekiguchi K, Tanaka M, Osaki M, Shishido C, Hasegawa N and Cheng S 2010 Application of model-based library approach to photoresist pattern shape measurement in advanced lithography *Proc. SPIE* **7638** 76382O

[41] Babin S, Bay K and Machin M 2010 Model based analysis of SEM images to automatically extract linewidth, edge roughness, and wall angle *Proc. SPIE* **7638** 76380R

[42] Villarrubia J S and Ding Z J 2009 Sensitivity of scanning electron microscope width measurements to model assumptions *J. Micro/Nanolithogr. MEMS MOEMS* **8** 033003

[43] Reimer L 1998 *Electron Scattering and Diffusion* (Berlin: Springer)

[44] Shimizu R and Ding Z J 1992 Monte Carlo modeling of electron-solid interactions *Rep. Prog. Phys.* **55** 487

[45] Joy D C 1995 *Monte Carlo Modeling for Electron Microscopy and Microanalysis* (Oxford: Oxford University Press)

[46] Dapor M 2020 *Transport of Energetic Electrons in Solids: Computer Simulation with Applications to Materials Analysis and Characterization* (Berlin: Springer Nature)

[47] Zou Y B, Mao S F, Da B and Ding Z J 2016 Surface sensitivity of secondary electrons emitted from amorphous solids: calculation of mean escape depth by a Monte Carlo method *J. Appl. Phys.* **120** 235102

[48] Ding Z J and Shimizu R 1996 A Monte Carlo modeling of electron interaction with solids including cascade secondary electron production *Scanning* **18** 92

[49] Ding Z J, Li H M, Goto K, Jiang Y Z and Shimizu R 2004 Energy spectra of backscattered electrons in Auger electron spectroscopy: comparison of Monte Carlo simulations with experiment *J. Appl. Phys.* **96** 4598

[50] Ding Z J and Li H M 2005 Application of Monte Carlo simulation to SEM image contrast of complex structures *Surf. Interface Anal.* **37** 912

[51] Mao S F, Li Y G, Zeng R G and Ding Z J 2008 Electron inelastic scattering and secondary electron emission calculated without the single pole approximation *J. Appl. Phys.* **104** 114907

[52] Ding Z J, Tang X D and Shimizu R 2001 Monte Carlo study of secondary electron emission *J. Appl. Phys.* **89** 718

[53] Penn D R 1987 Electron mean-free-path calculations using a model dielectric function *Phys. Rev. B.* **35** 482

[54] Li Y G, Mao S F, Li H M, Xiao S M and Ding Z J 2008 Monte Carlo simulation study of scanning electron microscopy images of rough surfaces *J. Appl. Phys.* **104** 064901

[55] Mott N F 1929 The scattering of fast electrons by atomic nuclei *Phil. Trans. R. Soc.* A **124** 425

[56] Yamazaki Y 1977 Studies on electron scattering by mercury atoms and electron spin polarization detector PhD Thesis Osaka University, Japan

[57] Yang L H, Tőkési K, Da B and Ding Z J 2019 Determination of electron inelastic mean free path of three transition metals from reflection electron energy loss spectroscopy spectrum measurement data *Eur. Phys. J.* D **73** 21

[58] Yang L H, Tőkési K, Tóth J, Da B, Li H M and Ding Z J 2019 Optical properties of silicon and germanium determined by high-precision analysis of reflection electron energy loss spectroscopy spectra *Phys. Rev.* B **100** 245209

[59] Henke B L, Gullikson E M and Davis J C 1993 X-ray interactions: photoabsorption, scattering, transmission, and reflection at E = 50–30 000 eV, Z=1-92 *At. Data Nucl. Data Tables* **54** 181

[60] Palik E D 1998 *Handbook of Optical Constants of Solids* (New York: Academic)

[61] Walker C G, El-Gomati M M, Assa'd A M and Zadrazil M 2008 The secondary electron emission yield for 24 solid elements excited by primary electrons in the range 250–5000 eV: a theory/experiment comparison *Scanning* **30** 365

[62] Li H M and Ding Z J 2005 Monte Carlo simulation of secondary electron and backscattered electron images in scanning electron microscopy for specimen with complex geometric structure *Scanning* **27** 254

[63] Yue Y T, Li H M and Ding Z J 2005 Monte Carlo simulation of secondary electron and backscattered electron images for a nanoparticle-matrix system *J. Phys. D: Appl. Phys.* **38** 1966

[64] Zhang P, Wang H Y, Li Y G, Mao S F and Ding Z J 2012 Monte Carlo simulation of secondary electron images for real sample structures in scanning electron microscopy *Scanning* **34** 145

[65] Villarrubia J S, Vladár A E and Postek M T 2014 3D Monte Carlo modeling of the SEM: are there applications to photomask metrology? *Proc. SPIE* **9236** 923602

[66] Hussain A, Yang L, Mao S F, Da B, Tőkési K and Ding Z J 2021 Determination of electron backscattering coefficient of beryllium by a high-precision Monte Carlo simulation *Nucl. Mater. Energy* **26** 100862

[67] Cleary J G and Wyvill G 1988 Analysis of an algorithm for fast ray tracing using uniform space subdivision *Vis. Comput.* **4** 65

[68] Geuzaine C and Remacle J F 2009 Gmsh: a 3D finite element mesh generator with built-in pre- and post-processing facilities *Int. J. Numer. Methods Eng.* **79** 1309
[69] Khan M S S, Zou Y B, Li C and Ding Z J 2019 Monte Carlo simulation of secondary electron emission from wave-type structure *J. Univ. Sci. Technol.* C **49** 79
[70] Cazaux J 2005 Recent developments and new strategies in scanning electron microscopy *J. Microsc.* **217** 16
[71] Bronsgeest M S, Barth J E, Swanson L W and Kruit P 2008 Probe current, probe size, and the practical brightness for probe forming systems *J. Vac. Sci. Technol.* B **26** 949
[72] Tanaka M, Villarrubia J S and Vladár A E 2005 Influence of focus variation on linewidth measurements *Proc. SPIE* **5752** 144
[73] Zhang P, Mao S F and Ding Z J 2015 Monte Carlo study of the effective electron beam shape in scanning electron microscopic imaging *Eur. Phys. J. Appl. Phys.* **69** 30703